Rapid TAURUS for Relaxation-Based Color Magnetic Particle Imaging

M. Tunç Arslan, A. Alper Özaslan, Semih Kurt, Yavuz Muslu and Emine Ulku Saritas

Abstract— **Magnetic particle imaging (MPI) is a rapidly developing medical imaging modality that exploits the non-linear response of magnetic nanoparticles (MNPs). Color MPI widens the functionality of MPI, empowering it with the capability to distinguish different MNPs and/or MNP environments. The system function approach for color MPI relies on extensive calibrations that capture the differences in the harmonic responses of the MNPs. An alternative calibration-free x-space-based method called TAURUS estimates a map of the relaxation time constant, τ, by recovering the underlying mirror symmetry in the MPI signal. However, TAURUS requires a back and forth scanning of a given region, restricting its usage to slow trajectories with constant or piecewise constant focus fields (FFs). In this work, we propose a novel technique to increase the performance of TAURUS and enable τ map estimation for rapid and multi-dimensional trajectories. The proposed technique is based on correcting the distortions on mirror symmetry induced by time-varying FFs. We demonstrate via simulations and experiments in our in-house MPI scanner that the proposed method successfully estimates high-fidelity τ maps for rapid trajectories that provide orders of magnitude reduction in scanning time (over 300 fold for simulations and over 8 fold for experiments) while preserving the calibration-free property of TAURUS.**

Index Terms— **Magnetic particle imaging, color MPI, nanoparticle relaxation, mirror symmetry, x-space MPI, rapid trajectory.**

I. INTRODUCTION

MAGNETIC particle imaging (MPI) is a rapidly developing tracer-based medical imaging modality, which takes advantage of the non-linear response of magnetic nanoparticles (MNPs) under time-varying magnetic fields [1]–[5]. The leading applications of MPI include angiography [6], [7], stem cell tracking [8]–[10], inflammation imaging [11], [12], drug delivery [13], [14], traumatic brain injury imaging [15], cancer

imaging [16], and localized hyperthermia [17]. Color MPI is an emerging field within MPI, providing a means to distinguish different MNPs and/or MNP environments [18]. Color MPI offers various practical applications such as catheter tracking during cardiovascular interventions [19], [20], and identifying the characteristics of the environment such as viscosity [21]–[25] and temperature [26]–[28].

A standard MPI system utilizes three different magnetic fields to acquire an image of the spatial distribution of MNPs. First, a field free point (FFP) is created using a static selection field (SF) with strong spatial gradients. Then, a sinusoidal drive field (DF) is applied to move the FFP in a field-of-view (FOV). However, human safety concerns [29], [30] and/or hardware limitations constrain the region covered by the DF to a relatively small partial field-of-view (pFOV) around the FFP. Thus, additional low-frequency focus fields (FFs) are employed to shift the FFP in a wider FOV [31].

Depending on factors such as the magnetic material and core diameter, different MNPs are expected to have different MPI signal responses [3]. Additionally, differences in the environmental conditions such as temperature or viscosity can alter the relaxation behavior of the MNPs [32]. Recently, color MPI techniques have been proposed to take advantage of these differences to distinguish the MPI signals from different MNPs and/or environmental conditions. The first color MPI study targeted distinguishing MNPs using a system function reconstruction (SFR) approach [18]. SFR requires lengthy calibration measurements of a point source MNP at all voxel locations within a FOV [33], [34]. For the color MPI extension, an extended linear system of equations is solved to find the concentrations of different MNP types and/or MNPs in different environmental conditions for each voxel. SFR-based color MPI requires separate calibrations for each MNP type and/or environmental condition, further lengthening the calibration time [18], [19], [26], [35].

X-space-based color MPI techniques do not require calibration, but the resulting images are typically blurred by the point spread function (PSF) of the imaging system [36]. One approach is performing multiple measurements at different drive field (DF) amplitudes to differentiate the relaxation behaviors of MNPs [37]. Another approach is a relaxation time constant (τ) estimation method, abbreviated as TAURUS (τ estimation via Recovery of Underlying mirror Symmetry) [21], [24], [38]. Instead of estimating the concentrations of different MNPs like the SFR-based color MPI methods, TAURUS estimates a τ for each pFOV (or patch) within the image to

create a quantitative τ map. Importantly, it does not require any calibrations, multiple measurements, or prior knowledge about the MNPs to estimate the τ map. However, TAURUS relies on the underlying mirror symmetry of the MPI signal, which is valid only for trajectories that perform a strict back-and-forth scanning of each pFOV (e.g., a 1D DF applied together with constant FFs). This requirement restricts the usage of TAURUS to trajectories with constant or piecewise constant FFs, previously demonstrated for active scan times exceeding 2.5 minutes for a 0.8 cm×8 cm FOV [38]. Reducing the scan time can pave the way to real-time imaging applications of TAURUS [39].

In this work, we propose a novel technique that enables τ map estimation via TAURUS for rapid and multi-dimensional trajectories that can reduce the scan time by orders of magnitude. We first demonstrate how the time-varying FFs utilized in these trajectories distort the mirror symmetry of the MPI signal and propose a method to compensate for the FF-induced distortions. Additionally, we improve the performance of TAURUS by casting it as a weighted least squares (WLS-TAURUS) problem. With simulations and imaging experiments, we demonstrate that the proposed method is robust for a wide range of FF slew rates (SRs) and noise, successfully estimating τ maps for rapid multi-dimensional trajectories while preserving the calibration-free property of TAURUS. The proposed method provides high fidelity τ maps and orders of magnitude reduction in scanning time for TAURUS, demonstrated for over 300-fold reduction in simulations and over 8-fold reduction in experiments.

II. THEORY

A. Mirror Symmetry and TAURUS

In MPI, a simplifying approach is to model the relaxation effect as a Debye process, which can be expressed as a convolution relation [32]:

$$s(t) = s_{\text{adiab}}(t) * r_\tau(t), \tag{1a}$$

where

$$s_{\text{adiab}}(t) = \beta \dot{x}_s(t) \hat{\rho}(x)\big|_{x=x_s(t)}, \tag{1b}$$

$$r_\tau(t) = \frac{1}{\tau} e^{-t/\tau} u(t). \tag{1c}$$

Here, $*$ denotes convolution, $s(t)$ is the signal with relaxation, $s_{\text{adiab}}(t)$ is the adiabatic signal described by the Langevin model [40], and $r_\tau(t)$ is the relaxation kernel. In addition, $\hat{\rho}(x)$ is the MPI image blurred by the PSF, $x_s(t)$ is the FFP trajectory, $\dot{x}_s(t)$ is the FFP speed, and β is a constant that depends on system and MNP parameters [36], [40]. In the relaxation kernel, τ (sec) is the effective relaxation time constant of the MNP that explains the signal lag and $u(t)$ is the Heaviside unit step function [32].

TAURUS uses the underlying mirror symmetry of the adiabatic MPI signal to estimate the time constant τ [21], [38]. The mirror symmetry assumption is valid independent of the MNP type or distribution in space, as long as the signal is acquired during a back-and-forth FFP trajectory. Without loss of generality, consider the following trajectory with a 1D DF

in the z-direction together with constant FFs:

$$\boldsymbol{x}_s(t) = \begin{bmatrix} x(t) \\ y(t) \\ z(t) \end{bmatrix} = \underbrace{\begin{bmatrix} B_{F,x}/G_x \\ B_{F,y}/G_y \\ B_{F,z}/G_z \end{bmatrix}}_{\text{Focus Field}} + \underbrace{\begin{bmatrix} 0 \\ 0 \\ \frac{B_p}{G_z} cos(2\pi f_d t) \end{bmatrix}}_{\text{Drive Field}}. \tag{2}$$

Here, $B_{F,i}$ (T) are the constant FFs and G_i (T/m) are the SF gradients along each direction, respectively. In addition, B_p (T) and f_d (Hz) are the peak amplitude and the frequency of the DF, respectively. The size of pFOV covered by the DF alone is equal to $W_p = 2B_p/G_z$ [3]. We refer to this trajectory as the "piecewise trajectory" (PWT), as it utilizes piecewise constant FFs to scan a small pFOV. Then, $B_{F,i}$ are stepped to different values to cover the entire FOV piece by piece.

For PWT, we define the negative and positive signals as the half-cycle signals acquired during the back and forth portions of the FFP movement, respectively. Then, the mirror symmetry in $s_{\text{adiab}}(t)$ can be expressed as [21], [38]:

$$s_{\text{pos,adiab}}(t) = -s_{\text{neg,adiab}}(-t) = s_{\text{half}}(t). \tag{3}$$

For the signal with relaxation, however, this mirror symmetry is broken. Using Eqs. (1a) and (3), we can write:

$$s_{\text{pos}}(t) = s_{\text{half}}(t) * r_\tau(t) \tag{4a}$$

$$s_{\text{neg}}(t) = -s_{\text{half}}(-t) * r_\tau(t). \tag{4b}$$

The Fourier transforms of these signals and $r_\tau(t)$ are:

$$S_{\text{pos}}(f) = \mathcal{F}\{s_{\text{pos}}(t)\} = S_{\text{half}}(f)R_\tau(f), \tag{5a}$$

$$S_{\text{neg}}(f) = \mathcal{F}\{s_{\text{neg}}(t)\} = -S_{\text{half}}^*(f)R_\tau(f), \tag{5b}$$

$$R_\tau(f) = \mathcal{F}\{r_\tau(t)\} = \frac{1}{1 + i2\pi f\tau}. \tag{5c}$$

Here, $\mathcal{F}$ denotes Fourier transformation and superscript $*$ denotes complex conjugation. Next, τ can be computed in frequency domain as follows [21], [38]:

$$\tau(f) = \frac{S_{\text{pos}}^*(f) + S_{\text{neg}}(f)}{i2\pi f\left(S_{\text{pos}}^*(f) - S_{\text{neg}}(f)\right)}. \tag{6}$$

Ideally, $\tau(f)$ should be independent of frequency, f. However, the presence of noise or deviations from the model in Eq. (1a) can cause frequency dependency. To provide robustnesss against such non-idealities, a weighted average of $\tau(f)$ is computed using the magnitude spectrum $|S_{\text{pos}}(f)|$ as weights [38]. Once τ is computed, the mirror symmetric $s_{\text{adiab}}(t)$ can be recovered by deconvolving $s(t)$ with $r_\tau(t)$.
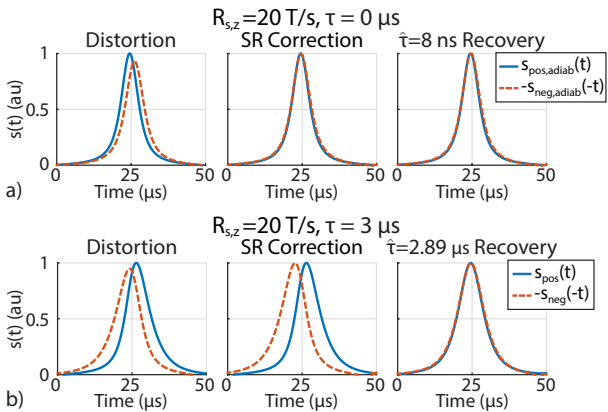
B. FF-Induced Distortions in Mirror Symmetry

Trajectories that contain time-varying FFs experience a distortion in mirror symmetry, even for the case of $s_{\text{adiab}}(t)$. Without loss of generality, consider the following FFP trajectory, with a 1D DF and a linearly ramping FF applied along the z-direction, and constant FFs in the x- and y-directions:

$$\boldsymbol{x}_s(t) = \begin{bmatrix} x(t) \\ y(t) \\ z(t) \end{bmatrix} = \begin{bmatrix} B_{F,x}/G_x \\ B_{F,y}/G_y \\ R_{s,z}t/G_z \end{bmatrix} + \begin{bmatrix} 0 \\ 0 \\ \frac{B_p}{G_z} cos(2\pi f_d t) \end{bmatrix}. \tag{7}$$

Here, $R_{s,z}$ (T/s) is the SR of the FF along the z-direction. As shown in Fig. 1, the positive and negative signals have matching amplitudes for $R_{s,z} = 0$. For $R_{s,z} = 20$ T/s, on the other hand, the amplitude is time varying due to the global
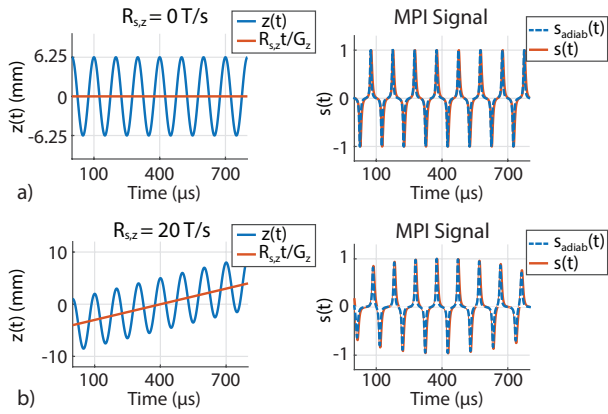
Fig. 1: Effects of a linearly ramping FF, demonstrating a time-varying signal amplitude at non-zero $R_{s,z}$. The FFP position, and the adiabatic and non-adiabatic signals for (a) $R_{s,z} = 0$ and (b) $R_{s,z} = 20$ T/s. Simulations utilized a point source MNP with $\tau = 3$ μs positioned at $z = 0$.

Fig. 2: FF-induced distortions on mirror symmetry at $R_{s,z} = 20$ T/s for (a) the adiabatic (i.e., $\tau = 0$) and (b) the non-adiabatic (for $\tau = 3$ μs) signals. After SR correction, the mirror symmetry is recovered for the adiabatic signal. After SR correction, TAURUS yields (a) $\hat{\tau} = 8$ ns and (b) $\hat{\tau} = 2.89$ μs.

FFP movement caused by the FF. The pFOV center moves by $R_{s,z}/(2f_dG_z)$ in half a DF period, so the FFP motion is no longer symmetrical around the pFOV center. In addition, the trajectory speed is different for the positive and negative signals, which further distorts the mirror symmetry in $s_{\text{adiab}}(t)$.

In Fig. 2.(a), the positive and mirrored negative signals for $s_{\text{adiab}}(t)$ (i.e., for $\tau = 0$) are plotted, showing the FF-induced distortions on mirror symmetry. The SR along the z-axis causes a lag between these two signals and a mismatch between their amplitudes.

C. SR Correction for Recovering Mirror Symmetry

For accurate τ estimations, we propose an SR correction method to correct the FF-induced distortions and recover the mirror symmetry in $s_{\text{adiab}}(t)$. First, we assume that the FFP speed is dominated by the DF for the majority of the FFP

motion. For Eq. (7), this assumption can be expressed as:

$$\max\left\{\left|\frac{d}{dt}\left(\frac{B_p}{G_z}cos(2\pi f_d t)\right)\right|\right\} \gg \left|\frac{d}{dt}\left(\frac{R_{s,z}}{G_z}t\right)\right|, \quad (8a)$$

$$B_p 2\pi f_d \gg R_{s,z}. \quad (8b)$$

Here, $\gg$ indicates at least an order of magnitude difference between the left- and right-hand sides of the inequality. Under this assumption, the overall effect of the FF can be approximated as a global time shift and a global amplitude scaling between the positive and negative signals.

A closed-form expression for the FF-induced time shift, Δt, can be found by solving the following equation:

$$z(t_0) = z(t_0 + T/2 + \Delta t), \quad (9a)$$

$$t_0 = \underset{t}{\operatorname{argmax}}(|\dot{z}(t)|), \quad t \in [0, T/2]. \quad (9b)$$

Here, $T = 1/f_d$ is the period of the drive field and t_0 is the time point during the first negative half-cycle at which the FFP speed is maximum. Without loss of generality, consider the trajectory in Eq. (7), where t_0 can be found as $1/(4f_d)$. For the same trajectory, Eq. (9a) can be expressed as:

$$\frac{R_{s,z}t_0}{G_z} + \frac{B_p cos(2\pi f_d t_0)}{G_z} = \frac{R_{s,z}(t_0 + T/2 + \Delta t)}{G_z} + \frac{B_p cos(2\pi f_d(t_0 + T/2 + \Delta t))}{G_z}. \quad (10)$$

Inserting $t_0 = 1/(4f_d)$ gives:

$$B_p cos(\tfrac{\pi}{2}) = \frac{R_{s,z}}{2f_d} + R_{s,z}\Delta t + B_p cos(\tfrac{3\pi}{2} + 2\pi f_d \Delta t)), \quad (11)$$

which can be simplified to:

$$B_p sin(2\pi f_d \Delta t) + R_{s,z}\Delta t + \frac{R_{s,z}}{2f_d} = 0. \quad (12)$$

If $\Delta t \ll 1/f_d$, a first-order Taylor series expansion of sine yields:

$$\Delta t = \frac{-R_{s,z}}{2f_d(B_p 2\pi f_d + R_{s,z})}. \quad (13)$$

A more accurate solution can be computed, e.g., using a higher-order Taylor series expansion of sine.

Next, the amplitude scaling, α, can be expressed as the ratio of the FFP speeds at t_0 and $t_0 + T/2 + \Delta t$, which yields:

$$\alpha = \frac{|B_p 2\pi f_d cos(2\pi f_d \Delta t) + R_{s,z}|}{|-B_p 2\pi f_d + R_{s,z}|}. \quad (14)$$

Once Δt and α are computed using Eqs. (12)-(14), the positive signal can be kept the same and the proposed SR correction can be applied to the negative signal only, i.e.,

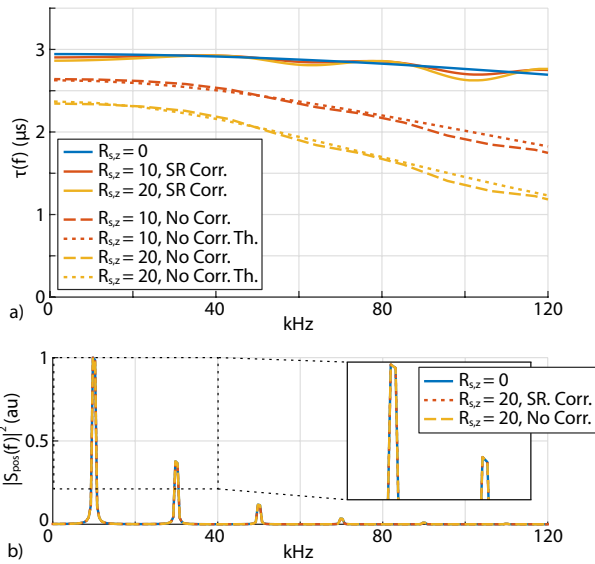$$S_{\text{pos,c}}(f) = S_{\text{pos,d}}(f), \quad (15a)$$

$$S_{\text{neg,c}}(f) = S_{\text{neg,d}}(f)e^{i2\pi\Delta t f}\alpha. \quad (15b)$$

Here, $S_{\text{pos,d}}(f)$ and $S_{\text{neg,d}}(f)$ are the SR-distorted negative and positive signals, respectively, and $S_{\text{pos,c}}(f)$ and $S_{\text{neg,c}}(f)$ are their corrected versions. Finally, Eq. (6) can be applied on the corrected signals to obtain SR-corrected estimation in frequency domain:

$$\tau(f) = \frac{S_{\text{pos,c}}^*(f) + S_{\text{neg,c}}(f)}{i2\pi f(S_{\text{pos,c}}^*(f) - S_{\text{neg,c}}(f))}. \quad (16)$$

TAURUS was originally proposed for the case of PWT, for which $R_{s,z} = 0$ and Eqs. (12)-(14) yield $\Delta t = 0$ and $\alpha = 1$, as expected. As $R_{s,z}$ increases, both Δt and α increase steadily. Importantly, both Δt and α are independent of the MNP

This article has been accepted for publication in IEEE Transactions on Medical Imaging. This is the author's version which has not been fully edited and content may change prior to final publication. Citation information: DOI 10.1109/TMI.2022.3195694

4   IEEE TRANSACTIONS ON MEDICAL IMAGING, VOL. XX, NO. XX, XXXX 2017

Fig. 3: (a) $\tau(f)$ for $R_{s,z} = 10$ and 20 T/s and (b) normalized power spectrum of the positive half-cycle before and after SR correction for $R_{s,z} = 20$ T/s. The SR-corrected $\tau(f)$ (solid lines) closely follows the reference case of $R_{s,z} = 0$, while the non-corrected $\tau(f)$ (dashed lines) shows increasing levels of underestimation at higher frequencies and closely follows the theoretical (Th.) $\tau_d(f)$ from Eq. 17 (dotted lines). The power spectra match closely. Simulations utilized a point source MNP with $\tau = 3 \, \mu$s.

parameters or the environmental conditions, and are purely dependent on the system and trajectory parameters.

Estimating τ without applying any SR correction would yield erroneous results. The estimation in frequency domain for the SR-distorted case, $\tau_d(f)$, can be expressed as follows (see Appendix VII for derivation):

$$\tau_d(f) = \frac{i2\pi f \tau d_+ + d_-}{i2\pi f \left(i2\pi f \tau d_- + d_+ \right)}, \tag{17}$$

where $d_\pm = \alpha \pm e^{-i2\pi\Delta t f}$. In the absence of FF-induced distortions (i.e., $R_{s,z} = 0$), $d_+ = 2$ and $d_- = 0$, yielding $\tau_d = \tau$, as expected. However, for increasing FF-induced distortions, τ_d diverges from τ.

In Fig. 2, the positive and negative signals of $s_{\text{adiab}}(t)$ (i.e., $\tau = 0$) and $s(t)$ (for $\tau = 3 \, \mu$s) are shown for $R_{s,z} = 20$ T/s. For accurate τ estimations, $s_{\text{adiab}}(t)$ should have a perfect mirror symmetry. However, due to the FF-induced distortions, the positive and the mirrored negative signals of $s_{\text{adiab}}(t)$ are shifted in opposite directions in time in Fig. 2.(a). Additionally, the amplitude of the negative signal is smaller than that of the positive signal. When SR correction is applied using Eq. (15), the mirror symmetry is recovered for $s_{\text{adiab}}(t)$. Computing τ using TAURUS yields $\hat{\tau} = 8$ ns in this case (i.e., within numerical error of zero, as expected). For $s(t)$ in Fig. 2.(b), the relaxation effect causes a separation of the positive and mirrored negative signals in the direction opposite to that caused by the SR. The relaxation effect also broadens the signal along the scanning direction. Directly computing τ using this distorted signal yields $\hat{\tau} = 1.85 \, \mu$s, a significant underestimation. After applying SR correction, the amplitudes

of the positive and negative signals match and the effective delay between them gets visibly larger. Then, computing τ for the SR-corrected signal gives $\hat{\tau} = 2.89 \, \mu$s, a close match to the actual value of $\tau = 3 \, \mu$s. Finally, applying deconvolution using this $\hat{\tau}$ recovers the underlying mirror symmetry of the MPI signal.

In Fig. 3, $\tau(f)$ and power spectrum are shown before and after SR correction for $R_{s,z} = 10$ and 20 T/s. Here, the results for $R_{s,z} = 0$ are provided as the references without any FF-induced distortions. As seen in Fig. 3.(a), the SR-corrected $\tau(f)$ closely follows the reference, whereas the non-corrected $\tau(f)$ shows increasing levels of underestimation at higher frequencies and closely follows the theoretical $\tau_d(f)$ from Eq. (17). Here, the ripple effect on SR-corrected $\tau(f)$ at $R_{s,z} = 10$ and 20 T/s is caused by the digital manipulations and temporal windowing of the signal. When the FFP speed is more strongly dominated by the DF (i.e., for smaller $R_{s,z}$), these ripples flatten and SR-corrected $\tau(f)$ converges to the reference. Nevertheless, since TAURUS applies an averaging of $\tau(f)$ weighted by the magnitude spectrum, the ripples in $\tau(f)$ at high frequencies have a relatively minor effect on the final estimated τ. In Fig. 3.(b), the normalized power spectrum of $s_{\text{pos}}(t)$ is shown, where there is negligible difference between the SR-corrected and non-corrected cases and the reference.

D. Rapid Color MPI Trajectories

The trajectory in Eq. (7) covers the FOV as a "line-by-line trajectory" (LLT), with overlapping pFOVs along the z-direction and discrete steps in the x- and y-directions. Due to the continuously ramping FF, this trajectory is already much faster than PWT. For example, for the FFP scanner used in this work with $G_z = 2.4$ T/m, even a relatively modest SR of $R_{s,z} = 4$ T/s corresponds to 0.83 m/s speed, which can cover a human-length line segment in approximately 2 seconds.

To cover a 2D or 3D FOV continuously, time-varying FFs, $B_{F,i}(t)$, can be utilized in all directions, i.e.,

$$\boldsymbol{x}_s(t) = \begin{bmatrix} B_{F,x}(t)/G_x \\ B_{F,y}(t)/G_y \\ B_{F,z}(t)/G_z \end{bmatrix} + \begin{bmatrix} 0 \\ 0 \\ \frac{B_p}{G_z}\cos(2\pi f_d t) \end{bmatrix}. \tag{18}$$

Defining $R_{s,i}(t) = \frac{d}{dt}B_{F,i}(t)$ as the SR for the FF along each direction, the assumption in Eq. (8) can be generalized as:

$$B_p 2\pi f_d \gg \max_t \{|R_{s,z}(t)|\}, \quad \forall t \in [0, T_s]. \tag{19}$$

Here, T_s is the total scan time. For example, for $B_p = 15$ mT, $f_d = 10$ kHz, and $R_{s,z} = 20$ T/s, Eq. (19) yields a ratio of 47 between the left- and right-hand sides of the inequality. Therefore, adopting the 20 T/s safety limit of MRI gradient fields to FFs [30], [41], we can conclude that the FFP speed is dominated by the DF for all practical purposes.

E. Weighted Least Squares TAURUS

The frequency domain division in Eq. (16) makes TAURUS susceptible to division by a small number or zero under the presence of noise and interference. Therefore, we propose

casting Eq. (16) as a weighted least squares (WLS) problem by first expressing it as a vector relation:

$$\mathbf{a}\tau = \mathbf{b}, \tag{20}$$

where $\mathbf{a}, \mathbf{b} \in \mathbb{C}^{K \times 1}$ such that:

$$\mathbf{a} = i2\pi k\Delta f \big(S^*_{\text{pos,c}}(k\Delta f) - S_{\text{neg,c}}(k\Delta f) \big), \tag{21a}$$
$$\mathbf{b} = S^*_{\text{pos,c}}(k\Delta f) + S_{\text{neg,c}}(k\Delta f). \tag{21b}$$

Here, $k = 0, 1, ..., K - 1$ with $K = f_s/\Delta f$, where f_s is the sampling frequency and Δf is the resolution in frequency domain. WLS-TAURUS can then be written as:

$$\tau = (\mathbf{a}^{\text{H}}\mathbf{W}\mathbf{a})^{-1}\mathbf{a}^{\text{H}}\mathbf{W}\mathbf{b}, \tag{22}$$

where $\mathbf{W} \in \mathbb{R}^{K \times K}$ is a diagonal weighting matrix with $W_{k,k} = |S_{\text{pos,c}}(k\Delta f)|^2$, and the superscript H denotes Hermitian transpose. As seen in Fig. 3.(b), this weighting is similar to harmonic selection, but provides better generalization when the signal energy shows variations across harmonics depending on the MNP distribution, or when the signal energy spreads around the harmonics at high SRs. WLS-TAURUS avoids the problem of division by a small number or zero, and is expected to provide robustness against noise.

F. Signal Replication for Increased TAURUS Performance

In Eq. (16), directly using the SR-corrected positive and negative signals, $s_{\text{pos,c}}(t)$ and $s_{\text{neg,c}}(t)$, results in a poor frequency resolution of $\Delta f = 2f_d$ (i.e., the inverse of a half DF period). To improve the frequency resolution, each period of the SR-corrected signal was first replicated N_{rep} times, then concatenated with the positive signal on the right side for $s_{\text{pos,c}}(t)$ and with the negative signal on the left side for $s_{\text{neg,c}}(t)$ to yield the extended versions. This procedure improves the frequency resolution to $\Delta f = 2f_d/(2N_{\text{rep}} + 1)$.

Example extended signals and the corresponding $\tau(f)$ for N_{rep} values of 0 and 4 at $R_{s,z} = 20$ T/s are given Fig. 4.(a). Note that the underlying mirror symmetry feature still applies for these extended signals. Next, the effect of N_{rep} on the $\tau(f)$ and the power spectra is shown in Fig. 4.(b). As clearly seen in the power spectra, the frequency resolution increases as N_{rep} increases. In Fig. 4.(c), the performances of SR-corrected TAURUS and WLS-TAURUS are evaluated as a function of $N_{\text{rep}} \in [0, \ 10]$ for the noise-free case and for relatively low signal-to-noise ratios (SNRs) of 2 and 10. The estimation error as a function of N_{rep} indicates that $N_{\text{rep}} < 3$ results in poor performance especially at SNR = 2. The performances of TAURUS and WLS-TAURUS both converge to a constant level for $N_{\text{rep}} > 5$, independent of the noise level. Therefore, for the rest of this work, $N_{\text{rep}} = 6$ was utilized.

III. METHODS

A. Simulations

The MPI simulations were carried out using a custom toolbox in MATLAB (Mathworks, Natick, MA). The parameters were chosen to mimic the experiments performed on our in-house MPI system: $(-4.8, \ 2.4, \ 2.4)$ T/m SF gradients in x-, y- and z-directions, 1D DF along the z-direction with
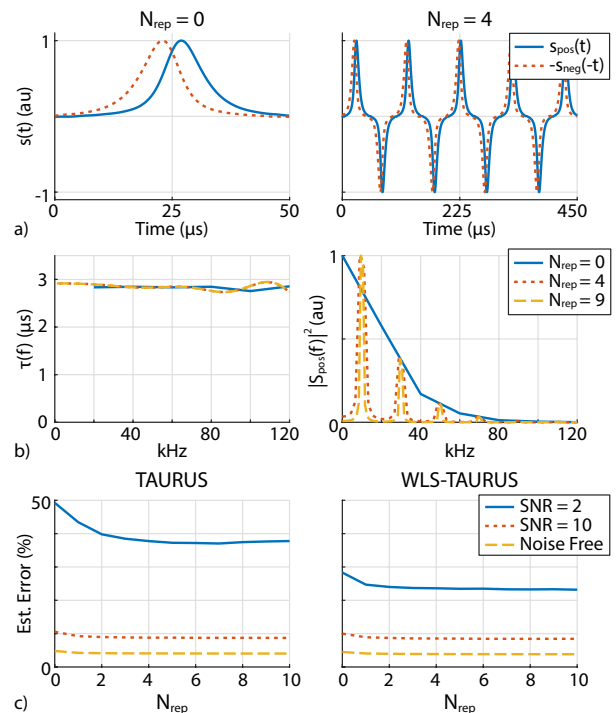

Fig. 4: Effects of signal replication on estimation error. (a) The positive and mirrored negative signals for $N_{\text{rep}} = 0$ (i.e., no replication) and $N_{\text{rep}} = 4$. (b) $\tau(f)$ and power spectra for different N_{rep} values. (c) Estimation error as a function of N_{rep} at different SNR levels for SR-corrected TAURUS and WLS-TAURUS.

$f_d = 10$ kHz and $B_p = 15$ mT, creating a pFOV of $W_p = 12.5$ mm. A homogeneous receive coil along the z-direction was utilized. The core MNP diameter, d, was assumed to be 25 nm, a realistic value based on the literature [42], [43]. To simulate the continuous-time nature of the physical world, the MNP responses were first generated at 100 MS/s, and then downsampled to 2 MS/s to generate the MPI signals. To emulate the direct feedthrough filtering utilized in the experiments, a zero-phase finite impulse response (FIR) high-pass filter (HPF) with a cut-off frequency of $1.5f_d$ was utilized. Finally, before applying TAURUS, the resulting signals were upsampled at 10 MHz to increase computational accuracy [38]. The details of each simulation are explained in detail below.

1) Slew Rate Robustness: The SR robustness of the proposed method was evaluated for $R_{s,z} \in [0, \ 20]$ T/s and $R_{s,x} \in [0, \ 20]$ T/s, where the estimation performances of the no correction and SR correction cases were compared, using WLS-TAURUS. The proposed SR correction in Eq. (15) incorporates a time-shift correction and an amplitude correction. Therefore, the performances of the no correction, only amplitude correction, only time-shift correction, and full SR correction cases were also evaluated for $R_{s,z} \in [0, \ 20]$ T/s, using WLS-TAURUS. For these simulations, a point source MNP distribution with $\tau = 3$ μs positioned at the origin with the core diameter of 25 nm was utilized.

2) Robustness against MNP Characteristics: Robustness of the proposed method against d and τ was evaluated for $d \in [15, \ 35]$ nm and $\tau \in [2, 4]$ μs, and SR-corrected
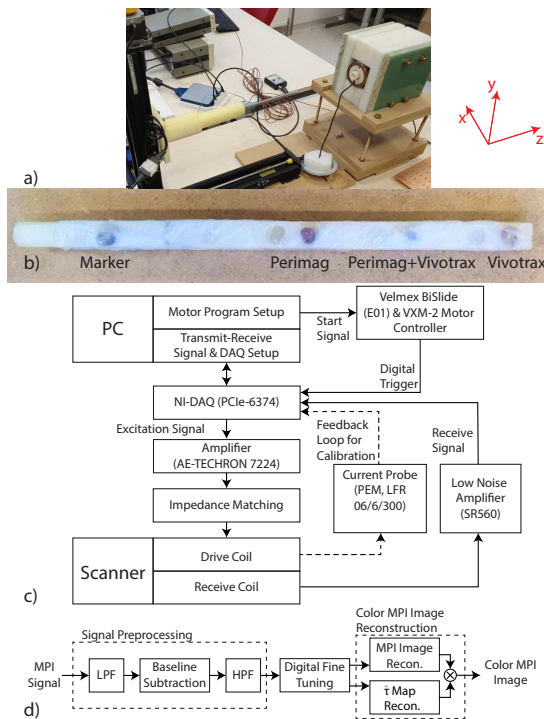
Fig. 5: (a) In-house FFP MPI scanner with $(-4.8, \ 2.4, \ 2.4)$ T/m SF gradients and 1D DF along the z-direction at 10 kHz. A three-axis linear actuator was utilized to move the FFP globally, instead of using FFs. (b) The imaging phantom contained Perimag, Vivotrax, their mixture, and a marker. (c) The flow diagram of the experimental process. A digital trigger from the VXM-2 motor controller was sent to the DAQ for synchronization. (d) The digital signal processing and image reconstruction stages for color MPI.

TAURUS and WLS-TAURUS were compared. The range for d was chosen based on the literature [42], and the range for τ was based on earlier TAURUS results using similar DFs [38]. These simulations utilized a point source MNP distribution positioned at the origin, with $R_{s,z} = 20$ T/s and $R_{s,x} = 0$ T/s.

3) Noise Robustness: Monte Carlo simulations were performed to compare the noise robustness of TAURUS and WLS-TAURUS, for $SNR \in [2, \ 20]$ and $R_{s,z} \in [0, \ 20]$ T/s. Accordingly, at a given SNR and $R_{s,z}$, simulations were repeated numerous times and the estimation errors for SR-corrected TAURUS and WLS-TAURUS were averaged across the repetitions. In each repetition, a different instance of white Gaussian noise with zero mean and a given standard deviation (STD) was added to the MPI signal. The noise STD was set as the maximum signal intensity (before direct feedthrough filtering) of the noise-free signal divided by the targeted SNR level. The number of repetitions was set to 10^4 for $SNR \le 5$, and 10^3 for $SNR > 5$ to ensure accurate estimation of performances. A point source MNP distribution with $\tau = 3$ μs positioned at the origin was utilized.

4) Color MPI Simulations: Finally, color MPI simulations were performed to evelute the performance of the proposed method. A phantom containing 6 MNP distributions with $\tau = [2, \ 2.4, \ 2.8, \ 3.2, \ 3.6 \ 4]$ μs was created. Each MNP distribution had a size of 2 mm$\times$2 mm. A 5 cm$\times$6 cm FOV in the x-z plane was scanned using 3 different trajectories:

Piecewise Trajectory (PWT): The FFs along the x- and z-directions were stepped to cover the FOV at 100×100 points in the x-z plane, providing 95.2% overlap between the consecutive pFOVs along the z-direction. An MPI signal of 10 ms duration was simulated at each point, resulting in an active scan time of 100 s for the entire trajectory.

Line-by-line Trajectory (LLT): A linearly ramping FF in the z-direction was utilized with $R_{s,z} = 4$ T/s to cover each line in 36 ms, with 98.7% overlap between the consecutive pFOVs along the z-direction. The FF along the x-direction was stepped to cover the x-direction at 100 equally spaced lines, resulting in an active scan time of 3.6 s.

2D Triangle Trajectory (2DTT): To cover the 2D FOV continuously, a linearly ramping FF in the z-direction was utilized. A triangle wave FF was applied along the x-direction, formulated as follows:

$$x(t) = \frac{\text{FOV}_x}{\pi} sin^{-1}\big(sin(2\pi f_\mathsf{T} t)\big), \ \ t \in [0, T_s). \qquad (23)$$

Here, $f_\mathsf{T} = R_{s,x}/(2\text{FOV}_x G_x)$ is the frequency of the triangle wave and scan time $T_s = \text{FOV}_z/(R_{s,z}/G_z)$. $R_{s,z} = 0.5$ T/s and $R_{s,x} = 20$ T/s were chosen to densely cover the whole FOV. There was no explicit overlap among the neighboring pFOVs due to the continuous movement along the x-direction. The resulting active scan time was 0.288 s.

Note that the active scan times listed above do not include the idle times of PWT and LLT during which the FFP position is stepped. For example, traversing each line back at the same SR of $R_{s,z} = 4$ T/s would automatically double the total scan time of LLT to 7.2 s. In contrast, 0.288 s active scan time for 2DTT is directly equal to the total scan time, as the whole FOV is scanned continuously in a single shot.

B. Imaging Experiments

Color MPI imaging experiments were performed on our in-house FFP MPI scanner shown in Fig. 5.(a), using 3 different trajectories. This scanner had $(-4.8, \ 2.4, \ 2.4)$ T/m SF gradients in the x-, y- and z-directions, and featured a free bore size of 1.9 cm and air cooling to prevent system heating. Both the drive and receive coils were oriented along the z-direction. To minimize the direct feedthrough, the receive coil was designed as a tunable 3-section gradiometric coil. Instead of utilizing FF coils to globally move the FFP, this scanner used a three-axis linear actuator (Velmex BiSlide), with a maximum speed of 38.1 mm/s in all axes, corresponding to $R_{s,z} = 0.091$ T/s. The other details of the scanner can be found in [24], [38].

The flow diagram of the experimental process is presented in Fig. 5.(c). For precise synchronization of the signal transmission/reception and the linear actuator movement, a digital trigger was sent from the VXM-2 motor controller of the actuator to a data acquisition card (DAQ) (NI PCIe-6374). The DAQ card sent the DF signal to the power amplifier (AE Techron 7224), which then sent it to the drive coil via an impedance matching circuitry tuned to $f_d = 10$ kHz. A current

probe (PEM LFR 06/6/300) was used for calibrating B_p. The received signal was pre-amplified using a low-noise amplifier (SRS SR560) and then sampled at 2 MS/s using the DAQ.

1) Trajectory Specifications: A 2D FOV of 0.7 cm×12.7 cm in the x-z plane was scanned using 3 different trajectories, shown in Fig. 6. The experiments utilized $f_d = 10$ kHz and $B_p = 15$ mT, resulting in a pFOV size of $W_p = 12.5$ mm.

PWT: The FOV was divided into 11×100 points in the x-z plane, providing 89.84% overlap between the consecutive pFOVs. A 150 ms signal was acquired for each pFOV, resulting in an active scan time of 165 s. Due to the idle times needed for actuator motion, the total scan time was approximately 46 min.

LLT: The x-direction was divided into 11 equally spaced lines. For the z-direction, the actuator was moved continuously at its maximum speed of 38.1 mm/s, corresponding to $R_{s,z} = 0.091$ T/s for $G_z = 2.4$ T/m. This relatively low $R_{s,z}$ resulted in 99.97% overlap between the consecutive pFOVs. Each line was covered in 3.46 s, resulting in an active scan time of 38 s. The total scan time was 76 s due to the idle times needed for the backward actuator movement along each line.

2DTT: A continuous triangle wave movement with $R_{s,x} = 0.061$ T/s and $R_{s,z} = 0.03$ T/s was applied using Eq. (23). The active scan time was 19.8 s, with no idle time.

For direct feedthrough compensation, baseline measurements were acquired before and after each line for PWT and LLT, and before and after the entire trajectory for 2DTT.

2) Phantom Preparation: As shown in Fig. 5.(b), an imaging phantom was prepared with 3 different samples, containing Perimag (Micromod GmbH), Vivotrax (Magnetic Insight Inc.) and their equal volume mixture. The samples were placed with 2.3 cm center-to-center separations. Each sample had 3 mm diameter in the x-z plane and contained a total volume of 20 μL. Perimag (17 mg Fe/mL undiluted concentration) was diluted 10.5 times to approximately equalize its signal level to that of Vivotrax (5.5 mg Fe/mL undiluted concentration). For computing signal timing (see Sec. III-B.4), an additional marker sample containing 10 μL undiluted Perimag was placed at a 4.6 cm separation from the leftmost sample.

3) Signal Preprocessing: As outlined in Fig. 5.(d), the received and baseline signals were individually low pass filtered using a zero-phase FIR filter with a cut-off frequency at 120 kHz to denoise the signal and remove the self-resonance of the receive coil at 280 kHz. Potential system drifts (e.g., due to heating or vibration) can cause slight delays between these two signals. This delay was negligibly small for PWT due to the short DF signals separated by extensive idle times that allowed system cooling. For LLT and 2DTT, the delay was more prominent due to the longer DF signals. The relative delay was computed by first upsampling the received and baseline signals at 100 MHz sampling rate, followed by a cross-correlation operation. The baseline signal was then time-shifted and subtracted from the received signal. Finally, the direct feedthrough at the fundamental harmonic was filtered out using a zero-phase FIR HPF with a cut-off frequency of $1.5 f_d$.

4) Digital Fine-Tuning of Signal Timing: TAURUS requires a precise (sub-sample level) adjustment of signal timing, as
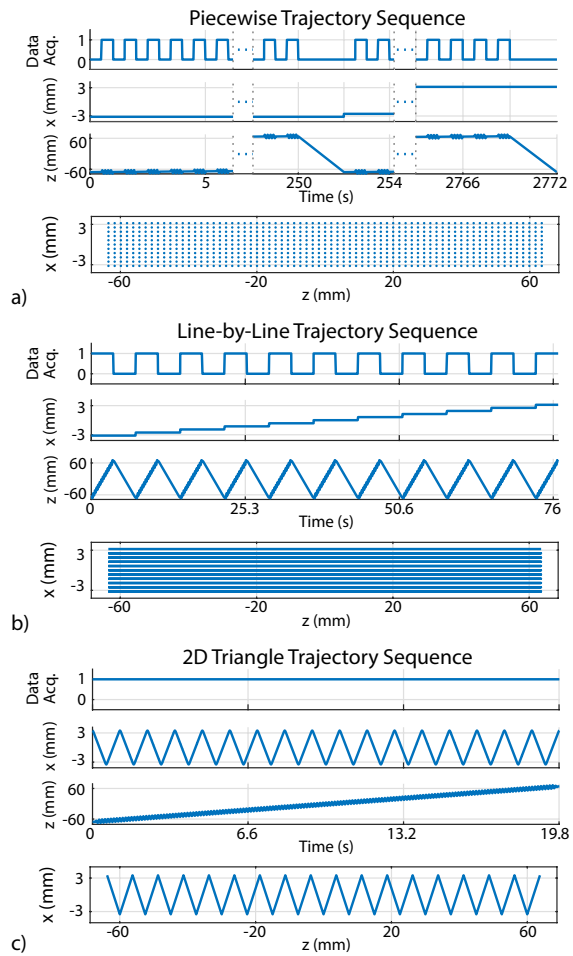

Fig. 6: Trajectories used in the imaging experiments, with 0.7 cm×12.7 cm FOV in the x-z plane. (a) PWT, with stepped x- and z- directions. (b) LLT, with stepped x-direction and a linear motion along z-direction. (c) 2DTT with a triangle-wave motion along x-direction and a linear motion along z-direction. The waveforms for the z-direction also show the superimposed 1D DF along the z-direction. The trajectories in the x-z plane do not reflect the DF.

unaccounted delays can cause a bias in $\hat{\tau}$. The signal timing, t_i, of the preprocessed signal was fine tuned using the marker signal. To achieve sub-sample precision, first the signal was upsampled at 100 MHz sampling rate. The tuning process took advantage of the underlying mirror symmetry: when $r_\tau(t)$ computed at the correct t_i is used to deconvolve the signal, the mirror symmetry should be achieved [38], i.e.,

$$\hat{t}_i = \underset{t_i}{\arg\min} \ \mathrm{MSE}(s_{\mathrm{pos,d}}(t), -s_{\mathrm{neg,d}}(-t)). \tag{24}$$

Here, $\hat{t}_i$ is the estimated signal timing that minimizes the mean square error (MSE) in mirror symmetry. In addition, $s_{\mathrm{pos,d}}(t)$ and $s_{\mathrm{neg,d}}(t)$ denote the positive and negative signals after deconvolution with $r_\tau(t)$ computed at t_i, respectively. Finally, the estimated $\hat{t}_i$ was applied to the entire signal. As outlined in Fig. 5.(d), the resulting signal is then fed to the image reconstruction step.
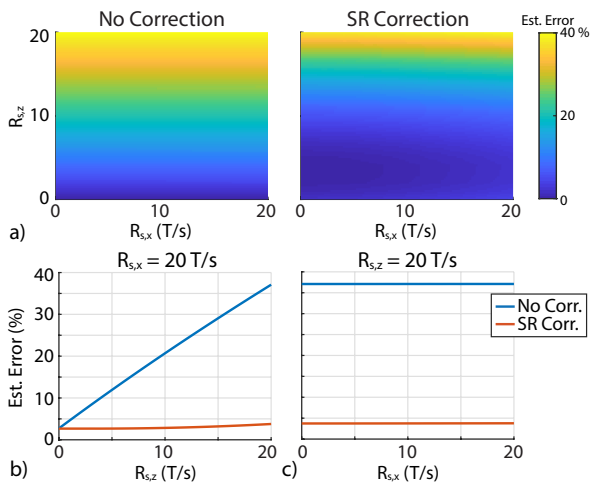
Fig. 7: SR robustness results. The estimation error (a) as a function of $R_{s,x}$ and $R_{s,z}$ for no correction and SR correction, (b) as a function of $R_{s,z}$ for $R_{s,x} = 20$ T/s, and (c) as a function of $R_{s,x}$ for $R_{s,z} = 20$ T/s. SR correction reduces the estimation error to below 3.6% at all $R_{s,z}$ and $R_{s,x}$ values.
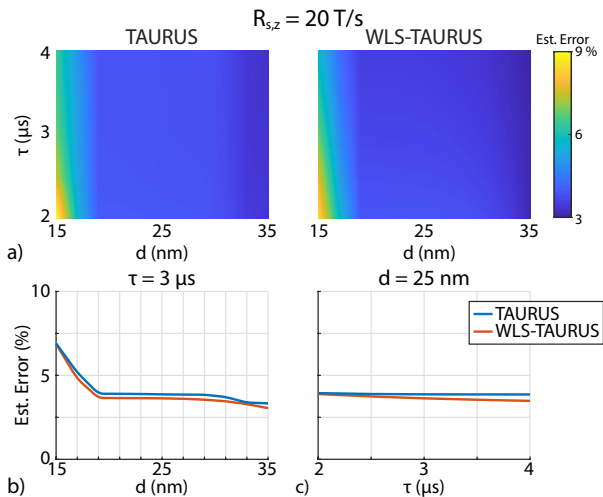

Fig. 8: Results for robustness against MNP characteristics. The estimation error for SR-corrected TAURUS and WLS-TAURUS (a) as a function of d and τ, (b) as a function of d for $\tau = 3\mu s$, and (c) as a function of τ for $d = 25$ nm. Both TAURUS and WLS-TAURUS show low estimation error for $d > 19$ nm.

C. Color MPI Image Reconstruction

Color MPI image reconstruction was composed of three steps: MPI image reconstruction, $\hat{\tau}$ map reconstruction, and color overlay formation.

MPI Image Reconstruction: The MPI images for PWT and LLT were reconstructed using Partial FOV Center Imaging (PCI) reconstruction [44]. PCI requires the pFOV centers to be aligned on a line and to have a high overlap percentage, and hence is suitable for PWT and LLT. Since 2DTT does not have any explicit overlap between pFOVs, PCI is not directly applicable. Taking advantage of the continuous signal acquisition of this trajectory, Harmonic Dispersion X-space (HD-X) reconstruction was utilized [45]. Since the data points
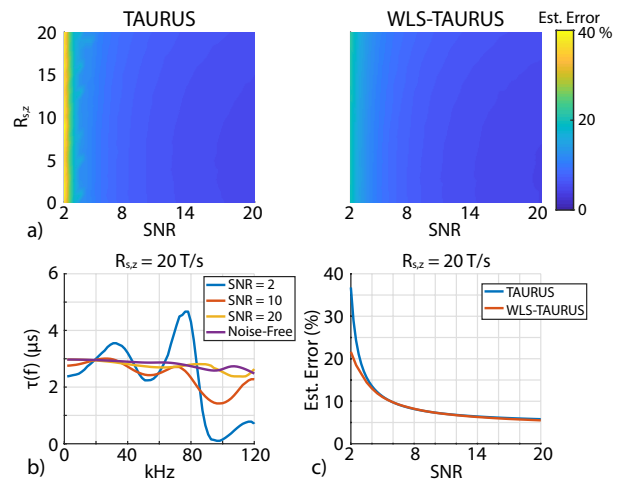
Fig. 9: Noise robustness results. (a) The estimation error for SR-corrected TAURUS and WLS-TAURUS with respect to SNR and $R_{s,z}$. (b) $\tau(f)$ for 4 different SNR levels at $R_{s,z} = 20$ T/s. (c) TAURUS vs. WLS-TAURUS with respect to SNR at $R_{s,z} = 20$ T/s. WLS-TAURUS shows improved robustness, especially for SNR < 5.

in 2DTT were on a non-Cartesian grid, an automated gridding algorithm for non-Cartesian MPI reconstruction was utilized on the HD-X data [46]. This gridding algorithm automatically tuned all reconstruction parameters, including the grid size. To reduce the blurring introduced by the gridding operation, the Cartesian output image was deconvolved with the gridding kernel using the Lucy-Richardson deconvolution [47]. The final reconstructed images had 500×600 pixels for the simulations and 200×2133 pixels for the imaging experiments.

$\hat{\tau}$ **Map Reconstruction**: After SR correction of each DF period, $\hat{\tau}$ was estimated using WLS-TAURUS with $N_{\text{rep}} = 6$. The estimated $\hat{\tau}$ values were placed on the corresponding pFOV center locations to form a $\hat{\tau}$ map. For 2DTT, the above-mentioned gridding algorithm was utilized to grid the $\hat{\tau}$ values to a Cartesian grid [46]. In the background regions, $\hat{\tau}$ can have unexpectedly high or low values due to low SNR. To ensure that these outlier $\hat{\tau}$ values do not contaminate the $\hat{\tau}$ map, the gridding kernel was reduced to one-fourth of that used during image reconstruction. Finally, the $\hat{\tau}$ map was interpolated to match the size of the MPI image. To suppress the noise-like $\hat{\tau}$ values in the background regions, the $\hat{\tau}$ map was multiplied with a binary mask of the MPI image, with a threshold of 10% of the maximum pixel intensity.

Color Overlay Formation: The $\hat{\tau}$ maps were overlayed with the reconstructed MPI images by multiplying the RGB pixel intensities of the two images, channel by channel.

IV. RESULTS

A. SR Robustness Results

The slew rate robustness of the proposed method is presented in Fig. 7.(a) as a function of $R_{s,z}$ and $R_{s,x}$, ranging between 0-20 T/s. Here, both the no correction and SR correction results utilized WLS-TAURUS. These results indicate that the estimation error does not depend on $R_{s,x}$, but is rather dominated by $R_{s,z}$ for the no correction case, reaching 37%
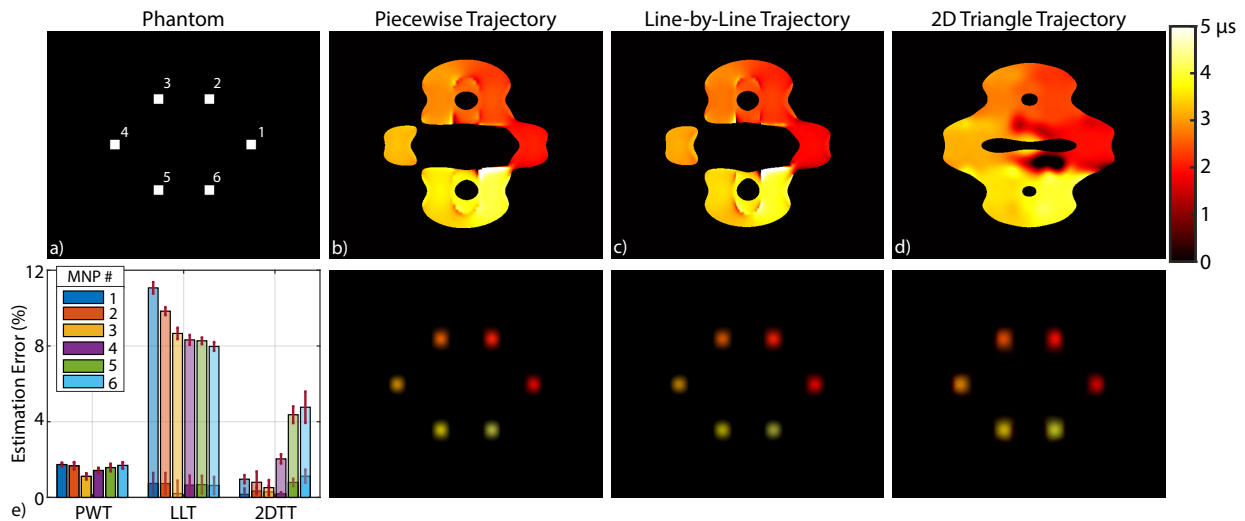
Fig. 10: Color MPI simulation results for 3 different trajectories. (a) The digital phantom with τ between 2-4 μs. The $\hat{\tau}$ maps (top row) and the corresponding color overlays (bottom row) for (b) PWT, (c) LLT, and (d) 2DTT, showing comparable performance despite their vastly different trajectory speeds. (e) The estimation performances, where the error bars denote the mean and STD of the estimation error in $\hat{\tau}$ for the non-corrected (semi-transparent bars) and SR-corrected (solid bars) cases. SR correction does not apply to PWT. SR correction provides a significant improvement in accuracy. 2DTT shows high accuracy estimation with fast scanning and dense coverage.

error at $R_{s,z} = 20$ T/s. SR correction successfully reduces the estimation error to below 3.6% at all $R_{s,z}$ and $R_{s,x}$ values tested. Figure 7.(b) shows the estimation error at $R_{s,x} = 20$ T/s as a function of $R_{s,z}$. Even at this large $R_{s,x}$, SR correction maintains a low estimation error at all $R_{s,z}$ values tested. Next, Fig. 7.(c) shows the estimation error at $R_{s,z} = 20$ T/s, displaying a less than 0.05% increase as a function of $R_{s,x}$ for both the no correction and SR correction cases.

The component-wise performances of the proposed SR correction method were also evaluated for $R_{s,z}$ ranging between 0-20 T/s (results not shown). Amplitude correction alone had minimal effect (less than 0.01%) on the estimation performance with respect to the no correction case. In contrast, time-shift correction alone provided a performance improvement that is only slightly (less than 0.06%) lower than the full SR correction case.

B. MNP Characteristics Robustness Results

The robustness against MNP characteristics for SR-corrected TAURUS and WLS-TAURUS are given in Fig. 8 for d ranging between 15-35 nm and τ ranging between 2-4 μs. Figure 8 shows comparable performances for both methods, with estimation errors below 3.7% for $d > 19$ nm, nearly independent of τ. The estimation error is approximately 8.6% at $d = 15$ nm and $\tau = 2$ μs, whereas it decreases down to 3.1% for TAURUS and 2.9% for WLS-TAURUS at $d = 35$ nm and $\tau = 4$ μs.

C. Noise Robustness Results

Noise robustness results for SR-corrected TAURUS and WLS-TAURUS are given in Fig. 9 for SNR ranging between 2-20 and $R_{s,z}$ ranging between 0-20 T/s. This analysis did not include $R_{s,x}$, as Fig. 7 indicated that $R_{s,x}$ does not have an

impact on the estimation error. As seen in Fig. 9.(a), the estimation error after SR correction is almost independent of $R_{s,z}$, but depends largely on the noise level. At high SNR levels, WLS-TAURUS provides a relatively small improvement over TAURUS. At low SNR levels, TAURUS shows high estimation errors, particularly for SNR < 5. In contrast, WLS-TAURUS maintains robustness against noise even at SNR = 2.

In Fig. 9.(b), SR-corrected $\tau(f)$ in Eq. (16) is plotted at 4 different SNR levels at $R_{s,z} = 20$ T/s. At SNR = 2, $\tau(f)$ shows large ripple-like deviations from the ideal value of $\tau = 3$ μs. These deviations increase at high frequencies, as the signal energy gets smaller and the computation of $\tau(f)$ gets dominated by noise. In addition, these ripples decrease at high SNR and converge to the noise-free case. As previously shown in Fig. 3, the ripples also increase with $R_{s,z}$. Hence, $\tau(f)$ shown for SNR = 2 and $R_{s,z} = 20$ T/s corresponds to the most challenging scenario.

Next, Fig. 9.(c) shows a direct comparison of TAURUS and WLS-TAURUS at $R_{s,z} = 20$ T/s as a function of SNR, where the improved noise robustness of WLS-TAURUS is clearly visible for SNR < 5. At SNR = 2, the estimation errors for TAURUS and WLS-TAURUS are 37% and 21%, respectively. At SNR = 20, the estimation errors fall down to 5.5% and 5.0% for TAURUS and WLS-TAURUS, respectively. In comparison, the estimation errors are 3.8% and 3.6% in the noise-free case for TAURUS and WLS-TAURUS, respectively.

D. Color MPI Simulation Results

Figure 10 shows the color MPI simulation results for 3 different trajectories. The digital phantom used in these simulations is displayed in Fig. 10.(a), with τ values between 2-4 μs. In Fig. 10.(b)-(d), the color overlays show comparable performance for PWT, LLT, and 2DTT, despite their vastly
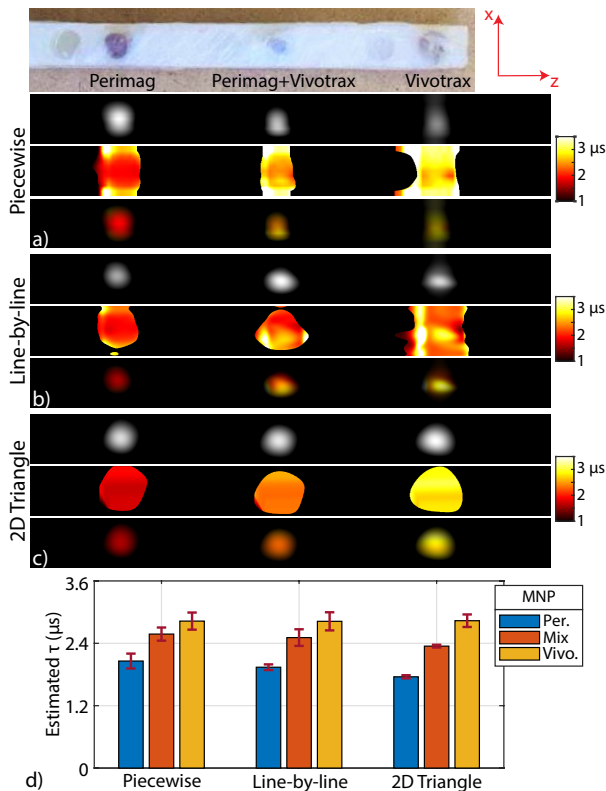
Fig. 11: Imaging experiment results. The reconstructed MPI images, $\hat{\tau}$ maps, and color overlays for (a) PWT, (b) LLT, and (c) 2DTT. $\hat{\tau}$ map for 2DTT is visibly smoother. (d) The estimated $\hat{\tau}$ for each sample, where the error bars denote the mean and STD within the FWHM region of the respective MPI image for that sample and trajectory. The displayed FOV is 0.7 cm×7.3 cm.

different speeds. The estimation performances are compared quantitatively in Fig. 10.(e), where the error bars denote the mean and STD of the estimation errors in $\hat{\tau}$ within the 2 mm×2 mm region for each MNP distribution. As seen in these results, 2DTT has the best performance, whereas LLT shows slightly improved performance over PWT. The mean estimation errors across all MNPs were 1.5±0.2%, 0.6±0.2% and 0.4±0.4% for PWT, LLT, and 2DTT, respectively. Figure 10.(e) also demonstrates the importance of SR correction: the estimations errors were 9.0±1.2% and 2.2±1.8% for the non-corrected cases of LLT and 2DTT, respectively. Here, consistent with the results in Fig. 7, the non-corrected case of LLT displayed a larger error due to utilizing higher $R_{s,z}$. Additionally, the results directly reflect the effect of trajectory density and $\hat{\tau}$ map fidelity for the SR-corrected cases. While LLT is denser than PWT along the z-direction, both LLT and PWT are relatively sparse along the x-direction. In contrast, 2DTT provides a dense coverage along both the x- and z-directions, resulting in improved estimation performance.

E. Imaging Experiment Results

Figure 11.(a)-(c) displays the imaging experiment results, showing the reconstructed MPI images, $\hat{\tau}$ maps, and color overlay images for 3 different trajectories. For PWT and LLT,

$\hat{\tau}$ shows a large variation along the x-direction due to the low trajectory density in that direction. For 2DTT, $\hat{\tau}$ map is visibly smoother with reduced variations along both x- and z-directions, as this trajectory is considerably denser than the other two trajectories. Since Vivotrax has worse full-width at half-maximum (FWHM) resolution than Perimag, its $\hat{\tau}$ values extend in a wider region along the z-direction [38].

The estimated $\hat{\tau}$ for each sample are given as bar plots in Fig. 11.(d). Here, the error bars denote the mean and STD of $\hat{\tau}$ of each sample within the FWHM region of the respective MPI image for that sample and trajectory. For PWT, the $\hat{\tau}$ values were 2.06±0.14 μs, 2.58±0.13 μs, and 2.83±0.16 μs for Perimag, mixture, and Vivotrax, respectively. For LLT, the $\hat{\tau}$ values were 1.94±0.05 μs, 2.51±0.16 μs, and 2.82±0.17 μs for Perimag, mixture, and Vivotrax, respectively. For 2DTT, the $\hat{\tau}$ values were 1.78±0.03 μs, 2.36±0.02 μs, and 2.83±0.12 μs for Perimag, mixture, and Vivotrax, respectively. These results indicate that $\hat{\tau}$ for Vivotrax is consistent, showing less than 1% variation across trajectories. This consistency is potentially due to the worse FWHM resolution of Vivotrax, which provides a paradoxical robustness against the low densities of PWT and LLT along the x-direction. In addition, $\hat{\tau}$ for Perimag is also consistent between PWT and LLT, with only 5.8% difference, as their densities match along the x-direction. In contrast, $\hat{\tau}$ for Perimag for 2DTT is approximately 13.6% and 8.2% lower than for PWT and LLT, respectively. These differences potentially stem from the substantially increased density of 2DTT along the x-direction. For each trajectory, $\hat{\tau}$ for the mixture closely matches the average of $\hat{\tau}$ for Perimag and Vivotrax, as expected [38].

Overall, these results indicate that 2DTT provides reliable $\hat{\tau}$ estimations thanks to its dense coverage, while also providing the shortest scan time among the tested trajectories.

V. DISCUSSION

In this work, we have proposed and experimentally demonstrated techniques that enable relaxation-based color MPI for rapid and multi-dimensional trajectories. The proposed SR correction method provides excellent robustness against FF-induced distortions for a wide range of SR values. Importantly, this method solely depends on the system and trajectory parameters. In addition, using a weighted least squares approach, WLS-TAURUS, successfully improves the noise robustness.

A. Alternative SR Correction Approaches

The proposed algorithm applies Δt time-shift and α scaling on the negative signal to align it with the positive signal. An alternative approach could be to apply $\Delta t/2$ time-shift and $\sqrt{\alpha}$ scaling on the negative signal and $\Delta t/2$ time-shift and $1/\sqrt{\alpha}$ scaling on the positive signal, so that they meet at the center of the half period. It can be shown that, in theory, this approach yields identical τ as the proposed approach given in Eq. (16). In practice also, it provides identical performance to the proposed SR correction, given that FF-induced shifts are within 1% of the DF period even at $R_{s,z} = 20$ T/s. Another approach could be to fully correct for the time-varying nature of the FF-induced distortions, so that the corrected $s_{adiab}(t)$

attains perfect mirror symmetry. However, such a correction would essentially stretch or compress one (or both) of the half-cycle signals, perturbing the temporal properties of the relaxation effect in Eq. (4). Since frequency-domain relations for TAURUS given in Eqs. (5)-(6) would no longer apply, this approach is not suitable for relaxation mapping. In contrast, the proposed SR correction preserves the relaxation effects within individual half cycles.

B. SR Robustness

The simulations presented in this work were based on our in-house MPI scanner, with both the drive and receive coils along the z-direction. As shown in Fig. 7, the SR correction is very robust against $R_{s,z}$ and does not depend on $R_{s,x}$. The latter effect stems from two reasons: the collinear PSF is relatively wide along the x-direction [40], and the DF is not along that direction. For the simulation parameters in this work, the collinear PSF has 1.8 mm and 2.1 mm FWHM along the z- and x-directions, respectively. Even for $R_{s,x} = 20$ T/s, the FFP moves approximately 0.2 mm along the x-direction in half the DF period, which is considerably smaller than the FWHM along that direction. Even in theory, reaching a comparable FWHM would require an effective MNP diameter greater than 55 nm. For the same reasons, we expect $R_{s,y}$ to have a similarly negligible effect.

C. Effects of MNP Diameter

According to the Langevin theory, increasing the MNP diameter or the SF gradients decreases the FWHM of the PSF in all directions [40]. Regardless, the MNP diameter is not expected to have any major effects on the τ estimation performance, as confirmed by the low estimation errors maintained for $d > 19$ nm in Fig. 8. First of all, SR correction is independent of the MNP parameters. Secondly, in terms of resolution, increasing the MNP diameter is equivalent to increasing G_z instead. The trajectory can still be kept identical if B_p and $R_{s,z}$ are increased at the same rate as G_z. Because the assumption in Eq. (19) remains unchanged, the estimation performance with respect to $R_{s,z}$ should not be affected.

With B_p and G_z fixed, the increase in estimation error for $d < 19$ nm is a result of the excessive widening of the PSF, which causes the MPI image to appear flat within the fixed pFOV size. In general, a flat MNP distribution can be problematic for τ estimation, as it causes the entire signal to fall on the fundamental harmonic. Then, the corresponding pFOV will have low signal after direct feedthrough filtering, despite having a non-zero pixel intensity in the reconstructed MPI image. A potential solution is to fill in the corresponding $\hat{\tau}$ regions using neighboring pFOVs, as proposed in [38]. Another alternative solution is to utilize active cancellation methods to preserve the fundamental harmonic [48], [49].

The effective d for the MNPs in the imaging experiments can be calculated using Fig. 11, where the FWHM values along the z-direction are 3.73 mm for Perimag and 4.40 mm for Vivotrax samples. Taking into account the 2.9 mm inner diameter of each sample together with the estimated $\hat{\tau}$ values, the effective MNP diameters are computed as 24.7 nm for

Perimag and 21.7 nm for Vivotrax. Note that these diameters are close to the 25 nm diameter used in the simulations, and are well above the 19 nm threshold mentioned above.

D. Resolution of τ Map

When creating the $\hat{\tau}$ map, a single $\hat{\tau}$ is estimated for each period of the signal and assigned to the center of the corresponding pFOV. Consequently, the resolution of $\hat{\tau}$ map is directly proportional to the trajectory density. For PWT, improving the resolution requires increasing the number of stepped points along both the x- and z-directions, increasing the scan time quadratically for a 2D FOV. For LLT, the resolution along the continuously scanned z-axis is sufficiently high and can be further improved by reducing $R_{s,z}$ (e.g., even at $R_{s,z} = 20$ T/s, the resolution along the z-axis is 0.83 mm for the parameters in this work). However, improving the resolution along the x-direction requires more lines to be scanned, which would increase the scan time linearly for a 2D FOV. In 2DTT, the resolution is considerably improved along the x-direction, but is position dependent. For a fixed scan time and FOV, $R_{s,z}$ and the number of pFOVs are also fixed. Then, a trade-off between the resolutions in the x- and z-directions can be achieved by adjusting $R_{s,x}$. By increasing the scan time and reducing $R_{s,z}$, the overall resolution of $\hat{\tau}$ map can be further improved in both directions.

It should be noted that controlling the trajectory density in a systematic fashion is challenging for 2DTT, as the trajectory parameters are coupled. For example, doubling f_d alone will double the density on the exact same trajectory. The same effect can also be achieved if $R_{s,x}$ and $R_{s,z}$ are both reduced to half with a doubling in scan time to cover the same FOV. However, in both cases, the off-trajectory points will not benefit from this seeming increase in density. In contrast, if we reduce only $R_{s,z}$ to half with a doubling in scan time, the trajectory itself will have twice as many triangles covering the same FOV. This time, the increased density will benefit the entire scanned FOV. Furthermore, the differences in scan time also need to be considered for a fair comparison of trajectories with respect to the noise level, as previously done in a thorough trajectory analysis of SFR-based image reconstruction [50]. Note that the color MPI simulations in Fig. 10 were noise-free and the experiments in Fig. 11 were performed using relatively high MNP concentrations showing negligible noise. Therefore, the differences in scan times did not cause any unfair bias in performance evaluations in this work. With that said, considering the coupling between the scan parameters, the effects of trajectory density on $\hat{\tau}$ map fidelity must be analyzed thoroughly with an appropriate definition of density, which remains an important future work.

E. Hardware and Safety Constraints on SR

In human-size applications of rapid TAURUS, both hardware and safety constraints will affect the imaging speed. The large imaging bore needed for human-size MPI scanners can require coils with large inductances [51], [52], with FF coil inductances in the mH range [53]. These large inductances can in turn limit the applicable SR, necessitating hardware

solutions to reduce the inductances [54]. For FF safety limits, we have adopted the 20 T/s safety limit of MRI gradient fields [41], given the similarity of their operating frequencies. In MPI, the dominating safety constraint for both DF and FF is magnetostimulation [29]. During simultaneous application of DF and FF, the safety limits and the allowable SR for FF can further reduce [30]. Therefore, 20 T/s can be considered as an upper limit for the SR of FF. Note that while the limitations on SR can hinder the imaging speed of MPI in general, they in turn make the speed assumption in Eq. (19) easier to satisfy.

F. Extension to Other Rapid MPI Trajectories

This work utilized constant SRs in both the simulations and the experiments. In fact, a constant but high SR (e.g., 20 T/s) is the worst-case scenario for FF-induced distortions. If the assumption in Eq. (19) is satisfied, extending the proposed method to time-varying SRs should not pose a challenge.

In this work, a 1D DF was utilized. Trajectories with multi-dimensional DFs, such as the Lissajous trajectory, can cover a 2D/3D pFOV in a relatively short scan time [50]. For such trajectories, the assumption in Eq. (19) has to be satisfied for each DF axis. Since TAURUS requires a back-and-forth scanning, the multi-dimensional DFs may need to be applied twice, once forward and once backward [38]. Note that, while x-space reconstruction was previously proposed for such trajectories [46], an experimental demonstration is yet to be shown. Extending TAURUS and x-space reconstruction to such multi-dimensional DFs remains an important future work.

VI. CONCLUSION

In this work, we have proposed a novel SR correction method to compensate for the FF-induced distortions in the underlying mirror symmetry of the MPI signal. The proposed method depends only on the system and scanning parameters, and enables high-fidelity relaxation map estimations via TAURUS for rapid and multi-dimensional trajectories. The performance is further boosted via a weighted least squares approach. The results show robustness against a wide range of SRs and noise, together with orders of magnitude reduction in scan time. The proposed rapid relaxation mapping method will have important applications in developing the functional imaging capabilities of MPI.

VII. APPENDIX

In this appendix, we derive Eq. (17). If we assume that SR correction fully recovers the mirror symmetry property, the SR-corrected signals should satisfy Eq. (5), i.e.,

$$S_{\text{pos,c}}(f) = S_{\text{half}}(f)R_\tau(f), \tag{25a}$$

$$S_{\text{neg,c}}(f) = -S_{\text{half}}^*(f)R_\tau(f). \tag{25b}$$

The non-corrected estimation can be expressed by applying Eq. (6) directly on the SR-distorted signal, i.e.,

$$\tau_d(f) = \frac{S_{\text{pos,d}}^*(f)+S_{\text{neg,d}}(f)}{i2\pi f\left(S_{\text{pos,d}}^*(f)-S_{\text{neg,d}}(f)\right)} \tag{26}$$

Using Eq. (15) and Eq. (25), $\tau_d(f)$ can be rewritten as follows:

$$\tau_d(f) = \frac{S_{\text{pos,c}}^*(f)+S_{\text{neg,c}}(f)e^{-i2\pi\Delta t f}/\alpha}{i2\pi f\left(S_{\text{pos,c}}^*(f)-S_{\text{neg,c}}(f)e^{-i2\pi\Delta t f}/\alpha\right)} \tag{27a}$$

$$= \frac{R^*(f)\alpha-R(f)e^{-i2\pi\Delta t f}}{i2\pi f\left(R^*(f)\alpha+R(f)e^{-i2\pi\Delta t f}\right)}. \tag{27b}$$

Inserting $R(f)$ as given in Eq. (5) and simplifying yields:

$$\tau_d(f) = \frac{\alpha(1+i2\pi f\tau)-e^{-i2\pi\Delta t f}(1-i2\pi f\tau)}{i2\pi f\left(\alpha(1+i2\pi f\tau)+e^{-i2\pi\Delta t f}(1-i2\pi f\tau)\right)}. \tag{28}$$

Finally, regrouping the terms and defining $d_\pm = \alpha\pm e^{-i2\pi\Delta t f}$, we get:

$$\tau_d(f) = \frac{i2\pi f\tau d_+ + d_-}{i2\pi f\left(i2\pi f\tau d_- + d_+\right)}. \tag{29}$$

VIII. ACKNOWLEDGMENTS

REFERENCES

[1] B. Gleich and J. Weizenecker, "Tomographic imaging using the nonlinear response of magnetic particles," *Nature*, vol. 435, no. 7046, pp. 1214–1217, 2005.

[2] P. W. Goodwill, E. U. Saritas, L. R. Croft, T. N. Kim, K. M. Krishnan, D. V. Schaffer, and S. M. Conolly, "X-space MPI: magnetic nanoparticles for safe medical imaging," *Adv. Mater.*, vol. 24, no. 28, pp. 3870–3877, 2012.

[3] E. U. Saritas, P. W. Goodwill, L. R. Croft, J. J. Konkle, K. Lu, B. Zheng, and S. M. Conolly, "Magnetic particle imaging (MPI) for NMR and MRI researchers," *J. Magn. Reson.*, vol. 229, pp. 116–126, 2013.

[4] B. Zheng, E. Yu, R. Orendorff, K. Lu, J. J. Konkle, Z. W. Tay, D. Hensley, X. Y. Zhou, P. Chandrasekharan, E. U. Saritas *et al.*, "Seeing SPIOs directly in vivo with magnetic particle imaging," *Mol. Imaging Biol.*, vol. 19, no. 3, pp. 385–390, 2017.

[5] L. Wu, Y. Zhang, G. Steinberg, H. Qu, S. Huang, M. Cheng, T. Bliss, F. Du, J. Rao, G. Song *et al.*, "A review of magnetic particle imaging and perspectives on neuroimaging," *AJNR Am. J. Neuroradiol.*, vol. 40, no. 2, pp. 206–212, 2019.

[6] I. Molwitz, H. Ittrich, T. Knopp, T. Mummert, J. Salamon, C. Jung, G. Adam, and M. Kaul, "First magnetic particle imaging angiography in human-sized organs by employing a multimodal ex vivo pig kidney perfusion system," *Physiol. Meas.*, vol. 40, no. 10, p. 105002, 2019.

[7] A. Mohtashamdolatshahi, H. Kratz, O. Kosch, R. Hauptmann, N. Stolzenburg, F. Wiekhorst, I. Sack, B. Hamm, M. Taupitz, and J. Schnorr, "In vivo magnetic particle imaging: angiography of inferior vena cava and aorta in rats using newly developed multicore particles," *Sci. Rep.*, vol. 10, no. 1, p. 17247, 2020.

[8] B. Zheng, T. Vazin, P. W. Goodwill, A. Conway, A. Verma, E. U. Saritas, D. Schaffer, and S. M. Conolly, "Magnetic particle imaging tracks the long-term fate of in vivo neural cell implants with high image contrast," *Sci. Rep.*, vol. 5, no. 1, p. 14055, 2015.

[9] K. Them, J. Salamon, P. Szwargulski, S. Sequeira, M. Kaul, C. Lange, H. Ittrich, and T. Knopp, "Increasing the sensitivity for stem cell monitoring in system-function based magnetic particle imaging," *Phys. Med. Biol.*, vol. 61, no. 9, pp. 3279–3290, 2016.

[10] Q. Wang, X. Ma, H. Liao, Z. Liang, F. Li, J. Tian, and D. Ling, "Artificially engineered cubic iron oxide nanoparticle as a high-performance magnetic particle imaging tracer for stem cell tracking," *ACS Nano*, vol. 14, no. 2, pp. 2053–2062, 2020.

[11] D. B. Mangarova, J. Brangsch, A. Mohtashamdolatshahi, O. Kosch, H. Paysen, F. Wiekhorst, R. Klopfleisch, R. Buchholz, U. Karst, M. Taupitz *et al.*, "Ex vivo magnetic particle imaging of vascular inflammation in abdominal aortic aneurysm in a murine model," *Sci. Rep.*, vol. 10, no. 1, p. 12410, 2020.

[12] P. Chandrasekharan, K. B. Fung, X. Y. Zhou, W. Cui, C. Colson, D. Mai, K. Jeffris, Q. Huynh, C. Saayujya, L. Kabuli *et al.*, "Non-radioactive and sensitive tracking of neutrophils towards inflammation using antibody functionalized magnetic particle imaging tracers," *Nanotheranostics*, vol. 5, no. 2, pp. 240–255, 2021.

[13] Z. W. Tay, P. Chandrasekharan, X. Y. Zhou, E. Yu, B. Zheng, and S. Conolly, "In vivo tracking and quantification of inhaled aerosol using magnetic particle imaging towards inhaled therapeutic monitoring," *Theranostics*, vol. 8, no. 13, pp. 3676–3687, 2018.

[14] X. Zhu, J. Li, P. Peng, N. Hosseini Nassab, and B. R. Smith, "Quantitative drug release monitoring in tumors of living subjects by magnetic particle imaging nanocomposite," *Nano Lett.*, vol. 19, no. 10, pp. 6725–6733, 2019.

[15] R. Orendorff, A. J. Peck, B. Zheng, S. N. Shirazi, R. M. Ferguson, A. P. Khandhar, S. J. Kemp, P. Goodwill, K. M. Krishnan, G. A. Brooks, D. Kaufer, and S. Conolly, "First in vivo traumatic brain injury imaging via magnetic particle imaging," *Phys. Med. Biol.*, vol. 62, no. 9, pp. 3501–3509, 2017.

[16] E. Y. Yu, M. Bishop, B. Zheng, R. M. Ferguson, A. P. Khandhar, S. J. Kemp, K. M. Krishnan, P. W. Goodwill, and S. M. Conolly, "Magnetic particle imaging: a novel in vivo imaging platform for cancer detection," *Nano Lett.*, vol. 17, no. 3, pp. 1648–1654, 2017.

[17] Z. W. Tay, P. Chandrasekharan, A. Chiu-Lam, D. W. Hensley, R. Dhavalikar, X. Y. Zhou, E. Y. Yu, P. W. Goodwill, B. Zheng, C. Rinaldi *et al.*, "Magnetic particle imaging-guided heating in vivo using gradient fields for arbitrary localization of magnetic hyperthermia therapy," *ACS Nano*, vol. 12, no. 4, pp. 3699–3713, 2018.

[18] J. Rahmer, A. Halkola, B. Gleich, I. Schmale, and J. Borgert, "First experimental evidence of the feasibility of multi-color magnetic particle imaging," *Phys. Med. Biol.*, vol. 60, no. 5, pp. 1775–1791, 2015.

[19] J. Haegele, S. Vaalma, N. Panagiotopoulos, J. Barkhausen, F. M. Vogt, J. Borgert, and J. Rahmer, "Multi-color magnetic particle imaging for cardiovascular interventions," *Phys. Med. Biol.*, vol. 61, no. 16, pp. N415–N426, 2016.

[20] J. Rahmer, D. Wirtz, C. Bontus, J. Borgert, and B. Gleich, "Interactive magnetic catheter steering with 3-d real-time feedback using multi-color magnetic particle imaging," *IEEE Trans. Med. Imaging.*, vol. 36, no. 7, pp. 1449–1456, 2017.

[21] M. Utkur, Y. Muslu, and E. U. Saritas, "Relaxation-based viscosity mapping for magnetic particle imaging," *Phys. Med. Biol.*, vol. 62, no. 9, pp. 3422–3439, 2017.

[22] C. Shasha, E. Teeman, and K. M. Krishnan, "Harmonic simulation study of simultaneous nanoparticle size and viscosity differentiation," *IEEE Magn. Lett.*, vol. 8, p. 1509405, 2017.

[23] M. Möddel, C. Meins, J. Dieckhoff, and T. Knopp, "Viscosity quantification using multi-contrast magnetic particle imaging," *New J. Phys.*, vol. 20, no. 8, p. 083001, 2018.

[24] M. Utkur, Y. Muslu, and E. Saritas, "Relaxation-based color magnetic particle imaging for viscosity mapping," *Appl. Phys. Lett.*, vol. 115, no. 15, p. 152403, 2019.

[25] S. Draack, M. Schilling, and T. Viereck, "Magnetic particle imaging of particle dynamics in complex matrix systems," *Phys. Sci. Rev.*, p. 20190123, 2021.

[26] C. Stehning, B. Gleich, and J. Rahmer, "Simultaneous magnetic particle imaging (MPI) and temperature mapping using multi-color MPI," *Int. J. Mag. Part. Imag.*, vol. 2, no. 2, p. 1612001, 2016.

[27] J. Zhong, M. Schilling, and F. Ludwig, "Magnetic nanoparticle temperature imaging with a scanning magnetic particle spectrometer," *Meas. Sci. Technol.*, vol. 29, no. 11, p. 115903, 2018.

[28] Y. Shi and J. B. Weaver, "Concurrent quantification of magnetic nanoparticles temperature and relaxation time," *Med. Phys.*, vol. 46, no. 9, pp. 4070–4076, 2019.

[29] E. U. Saritas, P. W. Goodwill, G. Z. Zhang, and S. M. Conolly, "Magnetostimulation limits in magnetic particle imaging," *IEEE Trans. Med. Imaging.*, vol. 32, no. 9, pp. 1600–1610, 2013.

[30] I. Schmale, B. Gleich, J. Rahmer, C. Bontus, J. Schmidt, and J. Borgert, "MPI safety in the view of MRI safety standards," *IEEE Trans. Magn.*, vol. 51, no. 2, p. 6502604, 2015.

[31] J. J. Konkle, P. W. Goodwill, E. U. Saritas, B. Zheng, K. Lu, and S. M. Conolly, "Twenty-fold acceleration of 3d projection reconstruction MPI," *Biomed. Tech. (Berl)*, vol. 58, no. 6, pp. 565–576, 2013.

[32] L. R. Croft, P. W. Goodwill, and S. M. Conolly, "Relaxation in x-space magnetic particle imaging," *IEEE Trans. Med. Imaging.*, vol. 31, no. 12, pp. 2335–2342, 2012.

[33] J. Rahmer, J. Weizenecker, B. Gleich, and J. Borgert, "Signal encoding in magnetic particle imaging: properties of the system function," *BMC Medical Imaging*, vol. 9, no. 1, p. 4, 2009.

[34] ——, "Analysis of a 3-d system function measured for magnetic particle imaging," *IEEE Trans. Med. Imaging.*, vol. 31, no. 6, pp. 1289–1299, 2012.

[35] P. Szwargulski, M. Wilmes, E. Javidi, F. Thieben, M. Graeser, M. Koch, C. Gruettner, G. Adam, C. Gerloff, T. Magnus *et al.*, "Monitoring intracranial cerebral hemorrhage using multicontrast real-time magnetic particle imaging," *ACS Nano*, vol. 14, no. 10, pp. 13 913–13 923, 2020.

[36] P. W. Goodwill and S. M. Conolly, "The x-space formulation of the magnetic particle imaging process: 1-d signal, resolution, bandwidth, SNR, SAR, and magnetostimulation," *IEEE Trans. Med. Imaging.*, vol. 29, no. 11, pp. 1851–1859, 2010.

[37] D. Hensley, P. Goodwill, L. Croft, and S. Conolly, "Preliminary experimental x-space color MPI," in *5th International Workshop on Magnetic Particle Imaging (IWMPI)*.   IEEE, 2015, p. 1.

[38] Y. Muslu, M. Utkur, O. B. Demirel, and E. U. Saritas, "Calibration-free relaxation-based multi-color magnetic particle imaging," *IEEE Trans. Med. Imaging.*, vol. 37, no. 8, pp. 1920–1931, 2018.

[39] M. T. Arslan and E. U. Saritas, "Rapid TAURUS for real-time color MPI: A feasibility study," *Int. J. Mag. Part. Imag.*, vol. 8, no. 1 Suppl 1, p. 2203060, 2022.

[40] P. W. Goodwill and S. M. Conolly, "Multidimensional x-space magnetic particle imaging," *IEEE Trans. Med. Imaging.*, vol. 30, no. 9, pp. 1581–1590, 2011.

[41] International Commission on Non-Ionizing Radiation Protection, "Medical magnetic resonance (MR) procedures: protection of patients," *Health Phys.*, vol. 87, no. 2, pp. 197–216, 2004.

[42] Z. W. Tay, D. W. Hensley, E. C. Vreeland, B. Zheng, and S. M. Conolly, "The relaxation wall: experimental limits to improving MPI spatial resolution by increasing nanoparticle core size," *Biomed. Phys. Eng. Express*, vol. 3, no. 3, p. 035003, 2017.

[43] R. M. Ferguson, A. P. Khandhar, S. J. Kemp, H. Arami, E. U. Saritas, L. R. Croft, J. Konkle, P. W. Goodwill, A. Halkola, J. Rahmer *et al.*, "Magnetic particle imaging with tailored iron oxide nanoparticle tracers," *IEEE Trans. Med. Imaging.*, vol. 34, no. 5, pp. 1077–1084, 2014.

[44] S. Kurt, Y. Muslu, and E. U. Saritas, "Partial fov center imaging (PCI): a robust x-space image reconstruction for magnetic particle imaging," *IEEE Trans. Med. Imaging.*, vol. 39, no. 11, pp. 3441–3450, 2020.

[45] S. Kurt, V. Abdulla, and E. U. Saritas, "Multi-dimensional harmonic dispersion x-space MPI," *Int. J. Mag. Part. Imag.*, vol. 6, no. 2 Suppl 1, p. 2009062, 2020.

[46] A. Ozaslan, A. Alacaoglu, O. Demirel, T. Çukur, and E. Saritas, "Fully automated gridding reconstruction for non-cartesian x-space magnetic particle imaging," *Phys. Med. Biol.*, vol. 64, no. 16, p. 165018, 2019.

[47] R. J. Hanisch, R. L. White, and R. L. Gilliland, "Deconvolution of Hubbles Space Telescope images and spectra," in *Deconvolution of images and spectra (2nd ed.)*, 1996, pp. 310–360.

[48] D. Pantke, N. Holle, A. Mogarkar, M. Straub, and V. Schulz, "Multifrequency magnetic particle imaging enabled by a combined passive and active drive field feed-through compensation approach," *Med. Phys.*, vol. 46, no. 9, pp. 4077–4086, 2019.

[49] B. Tasdelen, E. Yagiz, M. Utkur, A. R. Cagil, C. B. Top, E. Atalar, and E. U. Saritas, "Vector modulator based active compensation of direct feedthrough," *Int. J. Mag. Part. Imag.*, vol. 6, no. 2 Suppl 1, p. 2009065, 2020.

[50] T. Knopp, S. Biederer, T. Sattel, J. Weizenecker, B. Gleich, J. Borgert, and T. Buzug, "Trajectory analysis for magnetic particle imaging," *Phys. Med. Biol.*, vol. 54, no. 2, pp. 385–397, 2008.

[51] E. E. Mason, C. Z. Cooley, S. F. Cauley, M. A. Griswold, S. M. Conolly, and L. L. Wald, "Design analysis of an MPI human functional brain scanner," *Int. J. Mag. Part. Imag.*, vol. 3, no. 1, 2017.

[52] M. Gräser, F. Thieben, P. Szwargulski, F. Werner, N. Gdaniec, M. Boberg, F. Griese, M. Möddel, P. Ludewig, D. van de Ven, O. O. M. Weber, Woywode, B. Gleich, and T. Knopp, "Human-sized magnetic particle imaging for brain applications," *Nat. Commun.*, vol. 10, no. 1, p. 1936, 2019.

[53] C. B. Top, S. Ilbey, and H. E. Güven, "Electronically rotated and translated field-free line generation for open bore magnetic particle imaging," *Med. Phys.*, vol. 44, no. 12, pp. 6225–6238, 2017.

[54] A. A. Ozaslan, A. R. Cagil, M. Graeser, T. Knopp, and E. U. Saritas, "Design of a magnetostimulation head coil with Rutherford cable winding," *Int. J. Mag. Part. Imag.*, vol. 6, no. 2 Suppl 1, p. 2009063, 2020.